BeBeC-2026-D04

6-DIMENSIONAL UAV TRACKING WITH DIPOLE GREEN'S FUNCTIONS AND GROUND REFLECTIONS

Leon Steinhoff[1] and Armin Goudarzi[1]
[1]German Aerospace Center
Bunsenstrasse 10, 37073 Göttingen, Germany, leon.steinhoff@dlr.de

Abstract

Recent studies and surveys have shown the increasing use of drones (Unmanned Aerial Vehicles, UAVs) in many domains. However, the noise of UAVs is often perceived as annoying, prompting concerns regarding noise pollution and the need for novel acoustic certification guidelines. To measure UAV noise emissions in flight, their trajectory must be known. Given the integration of microphone arrays in existing sound measurement setups, acoustic tracking emerges as a reasonable method for UAV localization.

This paper proposes a beamforming-based approach for short-range 6-dimensional UAV tracking with a dipole Green's function and a mirror source model of the ground. The proposed method modifies the steering vector formulation by incorporating dipole directivity and coherent ground reflections directly into the acoustic transfer model. The dipole formulation is derived from the spatial derivative of the monopole Green's function, while the reflected contribution is modeled using an image-source approach. This enables a more realistic representation of the measured UAV sound field, particularly in near-ground measurement scenarios.

Conventional monopole and dipole beamforming are compared, with and without ground reflection. For evaluation, optical motion tracking results are serving as a "ground-truth". The reflection-aware dipole formulation provides the most accurate localization, demonstrating that the inclusion of dipole directivity and coherent ground reflections significantly improves acoustic UAV tracking accuracy in both translational and rotational degrees of freedom.

1 INTRODUCTION

The use of drones or UAVs (Unmanned Aerial Vehicles) has increased significantly in recent years. Forecasts predict that the market will grow to over 50 billion US dollars over the course of 2026 [8]. A notable rise in the deployment of UAVs can be observed particularly in sectors such as logistics, medical care, humanitarian aid, surveying, police and fire services, agriculture, photography and videography, recreational use and in urban air mobility (UAM).

These developments lead to increased exposure to aircraft noise that is perceived as disturbing. The noise generated by UAVs differs from the conventional aircraft noise produced by manned aviation [9]. Since most UAVs are significantly smaller and quieter than manned aircraft, they tend to be perceived only at shorter distances. Additionally, their distinct noise signature - characterized by higher dominant frequencies compared to manned aircraft - results in higher level of annoyance than lower-frequency sounds.

These are among the reasons why the European Union Aviation Safety Agency (EASA) considers noise to be the most important factor for the societal acceptance of UAVs [3]. Consequently, the sound emission of UAVs has to be measured and quantatized in order to validate the acoustic effects on the public and evaluate the annoyance of current and future UAVs. To enable standardized sound emission measurements, the EASA has published guidelines for drones [4]. However, these guidelines consider only a single radiation direction. Therefore, repeatable, comprehensive and extensive measurements of the sound emissions of different drones are of great importance for assessing societal acceptance and for developing certification processes.

Approaches for measurement methods to capture the directional sound radiation of flying UAVs have already been published [6, 7, 11]. For this, the measurement of the trajectory is indispensable. To determining the position of the drone, measuring the three orientation angles is essential for accurately characterizing directional sound radiation during complex flight maneuvers, since changes in flight attitude also alter the relative direction to the microphones. In previous studies it was shown, that this six-degrees-of-freedom (6 DoF) tracking is possible by just using the recorded data from a microphone array [13]. Conventional beamforming, CLEAN-SC [12] and Functional Beamforming [2] were considered for this method.

In this study, a custom beamforming algorithm is proposed and tested against the previous study and an optical motion tracking system, representing the ”ground-truth”. The beamforming algorithm incorporates a reflection model of the ground and a dipole source model for the UAV to better capture the environmental conditions and source characteristics of the proposed measurement setup. The ground reflections are added, due to a hard concrete ground present during the measurements and the dipole characteristic is included because of findings of other researchers [6, 7, 11] and also own observations showing a dipole radiation profile for many UAVs in wide frequency ranges.

2 METHODOLOGY

To validate the improved tracking accuracy, the results of an optical motion tracking system are used. They are considered as a ”ground-trouth” measurement, as optical motion tracking is a well-established technique with proven accuracy, especially when combined with precise camera calibration. For a meaningful validation the tracking algorithm is tested on real data obtained during an experimental measurement campaign with realistic flight conditions. The experimental setup as well as the individual methodologies for optical and acoustic tracking are given in details in the following subsections.

2.1 Experimental Setup

The measurements were conducted at the National Experimental Test Center for Unmanned Aviation at Magdeburg-Cochstedt Airport, as illustrated in Fig. 1. The setup comprised two microphone arrays and an optical motion tracking setup.

Figure 1: Experimental setup on the apron of Cochstedt-Magdeburg Airport. The two sound sphere array frames as well as the tracking array (right) can be seen. The higher beams are for the cameras of the optical motion tracking system.

The first microphone array, referred to as the sound sphere array (SA), was designed to capture the directional sound radiation (sound sphere) of UAVs flying through the frames. It comprises 184 custom-built MEMS microphones arranged along two rectangular frames, each measuring 2 m in height and 3 m in width, with a spacing of 4.2 m between them. An equiangular microphone distribution was implemented to ensure uniform angular resolution, resulting in a denser spacing near the center of the frame bars compared to the edges. Data acquisition was performed using three custom measurement units providing a total of 192 channels at a sampling frequency of 192 kHz. Additional channels were used to record the camera trigger signal and an external reference microphone. The microphones were connected via distribution boxes, with 96 microphones installed on the first frame and 88 on the second.

In addition, a second array, the tracking array (TA), was used to determine the UAV trajectory. This array is based on a MEMS microphone module originally developed at DLR for wind tunnel experiments [5]. The tracking array consistes of 800 MEMS microphones distributed over an area of 2 m^2. The microphones are mounted on printed circuit boards and arranged in a planar configuration. The array plane was setup parallel to the trajectory of a straight flight through the frames of the sound sphere array. Data acquisition was handled by four Field Programmable Gate Array (FPGA) units, each processing 200 channels. The signals were initially sampled at 3.072 MHz and later downsampled to 192 kHz with 16-bit resolution. Synchronization with the optical system was achieved by recording the camera trigger signal via dedicated analog inputs.

The optical motion tracking system employed four Ximea xiQ MQ042MG-CM global shutter cameras, each equipped with a 1-inch monochrome sensor with a resolution of 2048 × 2048 pixels (4.2 MP) and a wide-angle lens of 6 mm focal length. The aperture was set to f/4 to balance image sharpness and brightness. The cameras were mounted above the measurement volume to ensure full coverage of the region between the frames. Each camera was equipped with a ring light to illuminate retro-reflective markers attached to the UAVs, enabling reliable detection under dark conditions. The illumination allowed for short exposure times of 500 μs (1/2000 s), effectively eliminating motion blur even for fast-moving UAVs.

A quadcopter UAV, manufactured by the Institute of Fluid Mechanics (LSTM) at FAU Erlangen–Nürnberg, was used as a test platform. It will be referred to as FAU-UAV from now on. Figure 2 shows the UAV.

Figure 2: Top view of the FAU-UAV quadcopter. It features a diagonal propeller distance of 49 cm, an empty mass of roughly 3 kg, and 15.5 in (39.4 cm) diameter propellers.

All experiments were carried out during nighttime conditions to minimize wind disturbances and environmental noise, while also ensuring suitable illumination conditions for the optical tracking system.

To compensate for optical distortions introduced by the wide-angle lenses, a checkerboard calibration was performed using a 19 × 19 pattern with a square size of 7.5 cm. In addition, the spatial positions of both the cameras and the microphone arrays were determined using an optical total station. This allowed for the accurate estimation of camera viewing angles and the consistent alignment of all cameras and microphone arrays within a common coordinate system. The origin of this coordinate system is defined at the center of the first microphone frame, with the x-axis oriented perpendicular to the frame plane, the y-axis directed toward the second frame, and the z-axis pointing vertically upward. Note that with this coordinate system the trajectory of a flying UAV can have negative z-values. The ground was measured at the xy-plane at z = -1.03 m. Temporal synchronization between the measurement systems was achieved by recording the camera trigger signal with both microphone arrays, ensuring consistent timing and enabling direct comparison of the tracking results.

To evaluate the spatial and temporal calibration, as well as the alignment between the acoustic and optical systems, a custom-built device generating a small electric arc was employed. This electric arc acted as both an acoustic and optical point source, allowing the reconstructed three-dimensional positions obtained from both measurement approaches to be directly compared. The device was triggered multiple times accross the whole capture volume of the optical motion tracking system. The positions of the electric arcs were determined using triangulation of the emitted light in the optical system and, for the acoustic arrays, by cross-correlation of the microphone signals. The resulting mean deviations between the optical reference and the sound sphere array (Δ_{SA}), as well as the tracking array (Δ_{TA}), are summarized for all spatial directions in Table 1.

Table 1: Accuracy of spacial alignment between the two acoustic systems and the camera system.

Dimension	Δ_{SA} [cm]	Δ_{TA} [cm]
x	0.51	4.47
y	2.39	3.43
z	1.29	0.96
total	2.76	5.72

2.2 Optical Motion Tracking

For optical tracking, a triangulation approach based on four cameras was applied. The three retro-reflective markers mounted on top of the UAV (see Fig. 2) appear as bright dots in the camera images due to LED illumination. After correcting for lens distortions through calibration, triangulation rays can be drawn from each camera to the detected marker positions, resulting in three rays per camera for every recorded frame. The UAV position and orientation are then estimated using a minimization algorithm that incorporates the known relative geometry of the markers q_i. Specifically, the algorithm determines the optimal rotation matrix R and translation vector $\overrightarrow{t}$ such that the transformed marker positions are as close as possible to the set of triangulation lines L_j. This is achieved by minimizing the sum of squared distances between the transformed marker positions and all triangulation lines, as defined in Eq. (1).

$$C_{op}(R,\overrightarrow{t}) = \sum_{i=1}^{3}\sum_{j=1}^{12}\left(\mathrm{dist}\left(R\bullet q_i + \overrightarrow{t}, L_j\right)\right)^2 \tag{1}$$

The optimization variables correspond to the six degrees of freedom of the UAV motion: the three translational components x, y, and z, represented by $\overrightarrow{t}$, and the three rotational components θ, ϕ and ψ, included in R, which describe pitch, roll, and yaw, respectively.

The UAV position is only computed for time steps at which all four cameras successfully detect all three markers. Since this condition is not always fulfilled, missing data points are reconstructed using spline interpolation and subsequent smoothing. The resulting optical tracking trajectory has 6 dimensions (x, y, z, θ, ϕ and ψ) and a sampling rate of 90 Hz. It is depicted as red curves in Fig. 6 and 7.

2.3 Acoustic Tracking

The acoustic trajectory of the UAV is determined by applying beamforming to consecutive time windows. The tracking array is used for that. To maintain consistency with the optical tracking data, a sampling rate of 90 Hz is used. Each beamforming window comprises 2048 samples, corresponding to a duration of approximately 0.01 seconds. An initial estimate of the UAV position is obtained using a coarse three-dimensional focus grid spanning the entire measurement volume. This grid contains 14,400 focal points with a spatial resolution of 5 points per meter and is evaluated using conventional frequency-domain beamforming. The location of the maximum value within this grid serves as the center for a refined, high-resolution cubic grid. This second grid has a side length of 1.2 meters and a resolution of 41 points per dimension, resulting in approximately 69,000 focal points, and is processed using the proposed adapted beamforming including dipole assumption and ground reflections. The increased resolution enables the identification of individual sound sources of the UAV in three-dimensional space, which is essential for estimating its attitude.

The dipole assumption and ground reflections are implemented as follows. Let $\mathbf{x}_m \in \mathbb{R}^3$, $m = 1,\dots,M$, denote the microphone positions and $\mathbf{r}$ a candidate source position. For each frequency f with wave number $k = 2\pi f/c$, the microphone data are summarized by the cross-spectral matrix (CSM)

$$\mathbf{C}(f) = \frac{1}{K}\sum_{q=1}^{K} \mathbf{p}_q(f)\mathbf{p}_q^{\mathrm{H}}(f). \tag{2}$$

Conventional beamforming evaluates the quadratic form

$$B(\mathbf{r},f) = \mathbf{w}^{\mathrm{H}}(\mathbf{r},f)\,\mathbf{C}(f)\,\mathbf{w}(\mathbf{r},f), \tag{3}$$

optionally after removing the CSM diagonal. In this work the physical transfer vector $\mathbf{h}(\mathbf{r},f)$ is converted to the steering vector using the Sarradj I formulation [10],

$$w_m(\mathbf{r},f) = \frac{h_m(\mathbf{r},f)}{M\,|h_m(\mathbf{r},f)|}. \tag{4}$$

Formulations I and IV are suitable for source localization because they preserve the correct map maximum position, whereas formulations II and III provide a more appropriate absolute source-level scaling. Since only the trajectory position is evaluated here, the absolute beamforming level is not used. Broadband maps are obtained by normalizing $B(\mathbf{r},f)$ per frequency and averaging over the selected frequency band.

For a free-field monopole, the transfer function is the spherical Green's function

$$h_m^{\mathrm{mono}}(\mathbf{r},f) = G(\mathbf{x}_m,\mathbf{r},f) = \frac{\exp(-\mathrm{i}kR_m)}{4\pi R_m}, \qquad R_m = \|\mathbf{x}_m - \mathbf{r}\|_2. \tag{5}$$

A dipole source with unit orientation vector $\mathbf{n}$ is modeled as the directional derivative of the monopole Green's function. With $\hat{\mathbf{R}}_m = (\mathbf{x}_m - \mathbf{r})/R_m$, this yields

$$h_m^{\text{dip}}(\mathbf{r}, f; \mathbf{n}) = \mathbf{n}^{\text{T}} \nabla_{\mathbf{r}} G(\mathbf{x}_m, \mathbf{r}, f) = (1 + \mathrm{i}kR_m) \frac{\exp(-\mathrm{i}kR_m)}{4\pi R_m^2} \left(\mathbf{n}^{\text{T}} \hat{\mathbf{R}}_m\right). \tag{6}$$

The dipole model therefore adds both the directivity factor $\mathbf{n}^{\text{T}}\hat{\mathbf{R}}_m$ and the derivative factor $(1 + \mathrm{i}kR_m)/R_m$.

A specular ground reflection is included with the image-source method. For a horizontal ground plane at arbitrary height $z = z_{\text{floor}}$, the mirrored source and mirrored dipole orientation are

$$\mathbf{r}' = (r_x, r_y, 2z_{\text{floor}} - r_z)^{\text{T}}, \qquad \mathbf{n}' = (n_x, n_y, -n_z)^{\text{T}}. \tag{7}$$

With energy reflection coefficient R_E and pressure reflection factor $\rho = \sqrt{R_E}$, the reflected transfer vectors become

$$h_m^{\text{mono,refl}}(\mathbf{r}, f) = G(\mathbf{x}_m, \mathbf{r}, f) + \rho\, G(\mathbf{x}_m, \mathbf{r}', f), \tag{8}$$

$$h_m^{\text{dip,refl}}(\mathbf{r}, f; \mathbf{n}) = h_m^{\text{dip}}(\mathbf{r}, f; \mathbf{n}) + \rho\, h_m^{\text{dip}}(\mathbf{r}', f; \mathbf{n}'). \tag{9}$$

$R_E = 0.9$ is chosen as this is the value stated in literature for a rough, concrete surface in higher frequency bands [1]. The four evaluated steering models (Eq. (5), (6), (8) and (9)), only differ in the transfer vector $\mathbf{h}$. All are normalized with the same Sarradj-I steering definition above before conventional beamforming.

An example beamforming result is shown in Fig. 3 as a two-dimensional slice through the finer, cubic grid, representing the summed and normalized frequencies in the range of 6 to 55 kHz. The dominant sound sources are the two interaction regions between the front and rear propeller circles. It can be seen that the conventional beamformer (Fig. 3a) has stronger pronounced side lobes, especially in the x-direction, rendering the sound sources as elongated and blurred points. The proposed algorithm (Fig. 3b) shows a clearer and sharper resolution of the sources.

For the final estimation of the UAV's position and attitude, a minimization approach smimilar to that used for optical tracking is employed. In this step, an acoustic model of the UAV is aligned with the sound source distribution obtained from the beamforming. The acoustic model consists of discrete source points, as illustrated in Fig. 4. Their spatial arrangement is designed to represent the appearance of dominant aeroacoustic sources in the beamforming results. Though the points are not directly derived from real aeroacoustic sound sources, but rather their appearance in the beamforming images, they can be associated with turbulent boundary layers along the propeller blades and interaction regions between the propellers. Two line structures are introduced in the interaction regions to account for the influence of point spread function (PSF) side lobes, which are especially pronounced along the x-axis, as mentioned before and visible in Fig. 3.

The acoustic model and associated processing parameters were optimized in a dedicated parameter study. This investigation identified the frequency range from 6 to 55 kHz as particularly suitable for accurate acoustic tracking. Furthermore, alternative beamforming techniques, such as Clean-SC [12] and Functional Beamforming [2], were evaluated and compared to conventional frequency-domain beamforming. Different formulations of the cost function used for

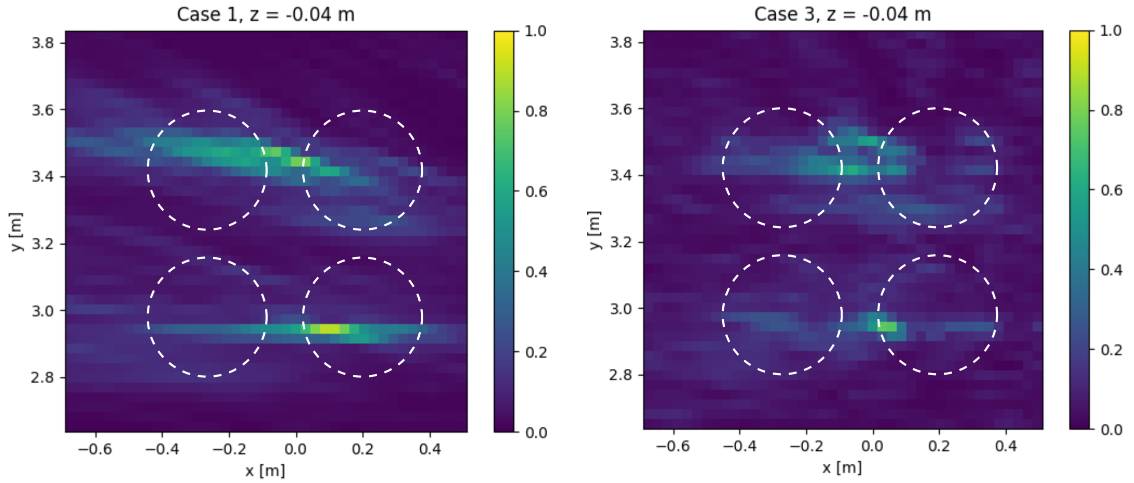

(a) 2D slice of the 3D conventional beamforming result of the FAU-UAV in flight. f_{Range} = 6-55 kHz; 2048 samples; f_s = 192 kHz.

(b) Beamforming result with dipole assumption and ground reflections. f_{Range} = 6-55 kHz; 2048 samples; f_s = 192 kHz.

Figure 3: Comparison of conventional (left) and dipole and reflection optimized (right) beamformer. The results are normalized as the array was not calibrated. The propeller circles of the true UAV position are shown in white.

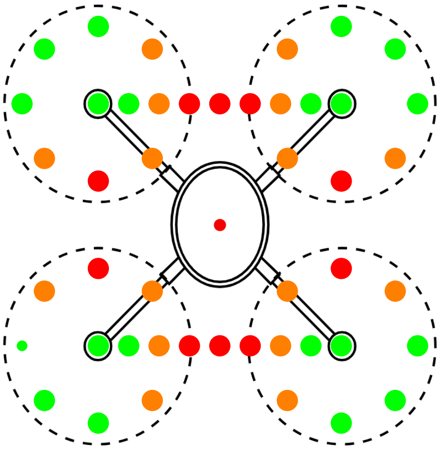

Figure 4: Overview of the acoustic models. These are used as sound models for acoustic tracking. The points each represent individual sound sources. The weighting of the points is indicated by color: green = 0.5, orange = 0.8, red = 1.

model alignment were also examined.

The selected cost function is defined in Eq. (10), where the model source points $\tilde{q}_i$ are transformed by a rotation matrix R and a translation vector $\overrightarrow{t}$. The cost is computed as a weighted sum of squared distances between the transformed model points and the beamforming-derived source locations b_j, with weighting factors w_j reflecting the relative amplitudes of the beamforming sources. In the chosen configuration, the use of 50 beamforming source points and 46 model points (see Fig. 4) provided the highest accuracy.

$$c_{ac}(R, \overrightarrow{t}) = \sum_{i=1}^{46} \min\left(\mathrm{dist}\left(R \bullet p_i + \overrightarrow{t}, b_j\right)^2 \cdot w_j\right) \tag{10}$$

3 RESULTS

Considering the ground reflections and a dipole source assumption, there are 4 cases which can be identified for validation: A monopole assumption without reflections (representing the basic and unmodified conventional beamformer), a monopole assumption with ground reflections, a dipole assumption without ground reflections and a dipole assumption with ground reflections. The sound propagation principle of the individual cases is shown in Fig. 5. The second case (named case 1.5 in Fig. 5) is neglected from further investigation as it produces similar results as the first case. The radiated energy of the direct sound path is the same as for the reflected path, resulting in slightly different values for the amplitude of the source but not the position. When incorporating the dipole assumption, the reflected sound path has significantly more energy than the direct path. Therefore, when assuming a dipole radiation, ground reflections make a significant diference. This leaves three cases to be evaluated.

The resulting acoustic tracking data, together with the optical motion tracking results, are presented in Fig. 6 and 7, as well as Table 2 and 3, for both translational and rotational degrees of freedom. As previously noted, the optical tracking data are interpolated and smoothed using spline interpolation. The same smoothing approach is applied to the acoustic trajectory, which exhibits comparatively higher noise levels. The resulting smoothed optical trajectory is shown as an orange curve and the smoothed acoustic trajectory as a black curve in the figures. Due to the limited field of view of the cameras, the optical data cover only the region between the two array frames, whereas the acoustic tracking can be extends over a larger spatial range. Nevertheless, the results are only shown within the overlapping region, as this way a direct comparison between both methods is possible.

The accuracy of the acoustic tracking is assessed by computing the deviations from the optical reference for all six degrees of freedom (Δx, Δy, Δz, $\Delta\theta$, $\Delta\phi$ and $\Delta\psi$). Based on these values, the mean translational and rotational errors are calculated using Eq. (11) and Eq. (12), respectively.

$$\Delta_{trans} = \sqrt{\Delta x^2 + \Delta y^2 + \Delta z^2} \tag{11}$$

$$\Delta_{rot} = \sqrt{\Delta\theta^2 + \Delta\phi^2 + \Delta\psi^2} \tag{12}$$

For the slow fly-through (3 m/s), case 3 achieves the best results. The acoustic data contain significantly more noise than the optical tracking data; however, with appropriate interpolation they provide sufficiently accurate approximations in all degrees of freedom. In particular, the rotational dimensions exhibit more noise. The accuracy and standard deviation (std) for both translatory and rotatory regimes are given in Table 2. With a mean error, or deviation from the optical tracking, of Δ_{trans} = 3.8 cm and Δ_{rot} = 6.5°, case 4 is the best performing, while the error for case 1 and 3 is roughly doubled. The achieved accuracy even exceeds the one of

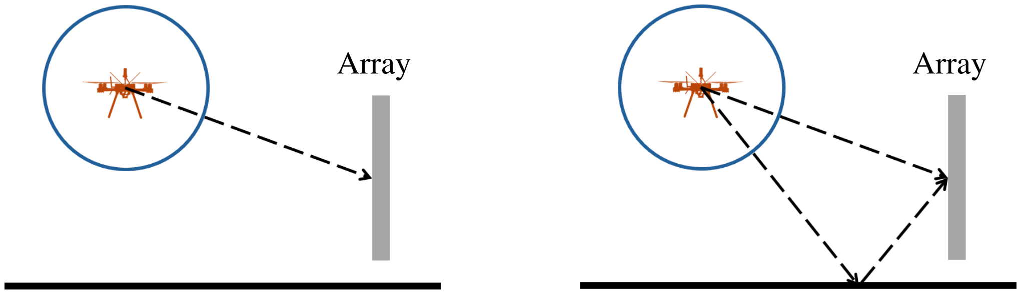

(a) Case 1: Monopole without reflections. *(b) (Case 1.5: Monopole with reflections)*

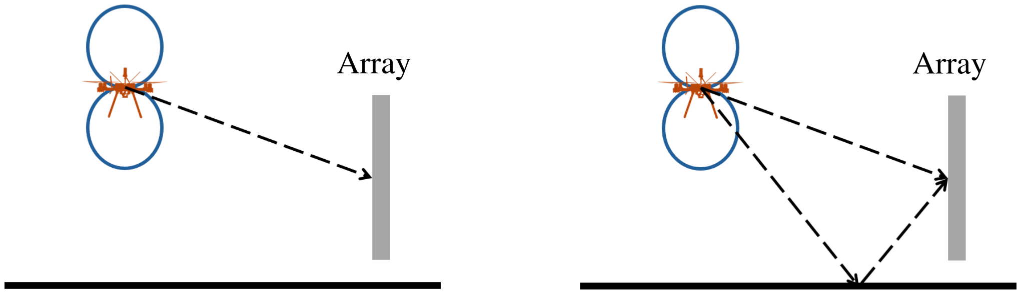

(c) Case 2: Dipole without reflections. *(d) Case 3: Dipole with reflections.*

Figure 5: Sound propagation for Cases 1–3 using monopole and dipole assumptions, with and without ground reflections. Cases 1 and 1.5 are identical except for the amplitude. This is why case 1.5 is not considered.

the measured translatory position of the tracking array (see Table 1), which indicates a barely improvable accuracy.

Table 2: Comparison of the mean error between the acoustic tracking and the opical motion tracking for a slow (3 m/s) fly-though.

Case 1: Monopole without reflections	Case 2: Dipole without reflections	Case 3: Dipole with reflections
$\Delta_{trans} = 7.27$ cm $\Delta_{rot} = 10.5°$ $std_{trans} = 1.52$ cm $std_{rot} = 6.97°$	$\Delta_{trans} = 7.46$ cm $\Delta_{rot} = 11.2°$ $std_{trans} = 2.04$ cm $std_{rot} = 2.81°$	$\Delta_{trans} = 3.80$ cm $\Delta_{rot} = 6.50°$ $std_{trans} = 2.06$ cm $std_{rot} = 3.11°$

For the fast fly-through (10 m/s) the results are similar. The accuracy in absolute terms is slightly lower than for the slow fly-through. It should also be noted that, due to the increased speed, there are fewer time instances at which results could be calculated. For the translational

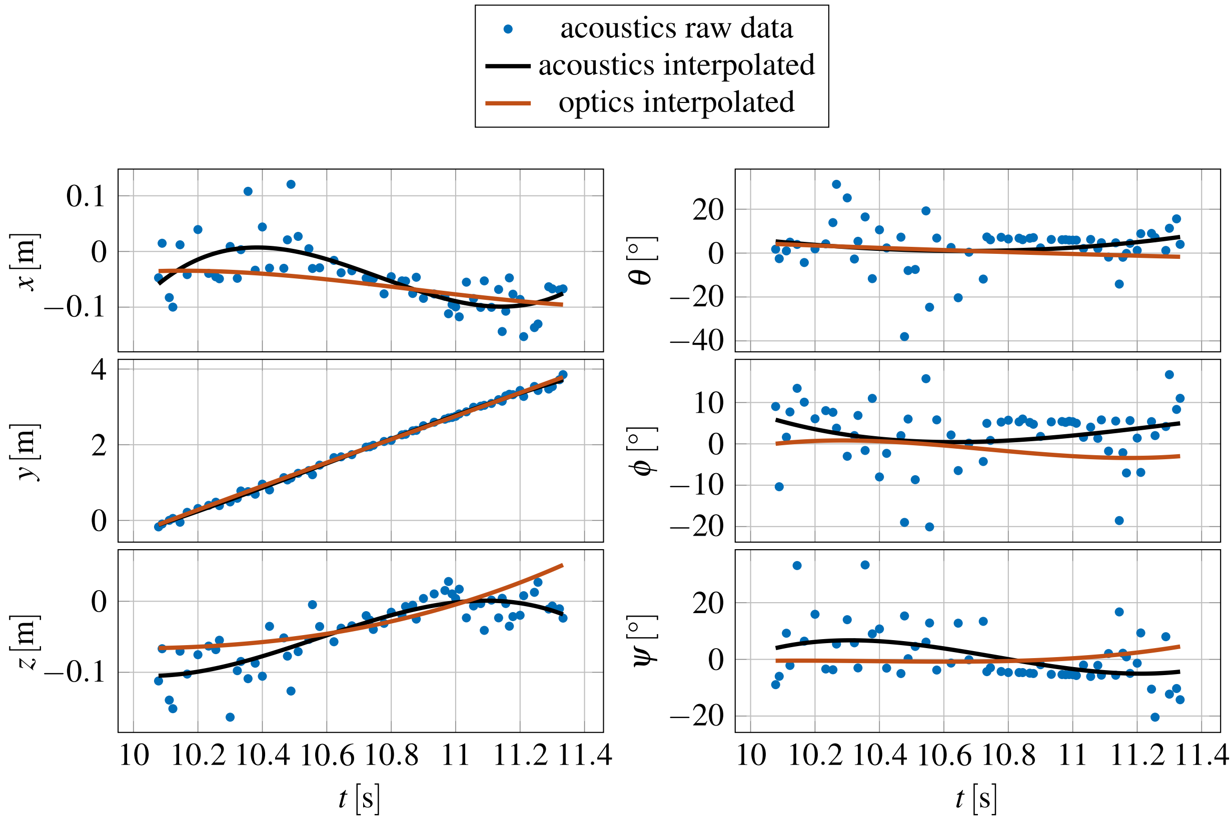

Figure 6: Translational (left) and rotational plot (right) of the acoustic tracking results (blue) and the "ground-truth" from the optical motion tracking (black) for a slow (3 m/s) fly-through.

accuracy, the error roughly doubles again when comparing case 3 with cases 1 and 2. In the rotational dimensions, however, the accuracy decreases only minimally. Figure 7 shows the translatory and rotatory plots for case 3, Table 3 shows the mean error and standard deviaton for all cases.

Table 3: Comparison of the mean error between the acoustic tracking and the opical motion tracking for a fast (10 m/s) fly-though.

Case 1: Monopole without reflections	Case 2: Dipole without reflections	Case 3: Dipole with reflections
Δ_{trans} = 10.2 cm Δ_{rot} = 9.42° std_{trans} = 4.64 cm std_{rot} = 2.67°	Δ_{trans} = 10.0 cm Δ_{rot} = 9.74° std_{trans} = 5.28 cm std_{rot} = 2.68°	Δ_{trans} = 5.05 cm Δ_{rot} = 8.17° std_{trans} = 3.60 cm std_{rot} = 5.33°

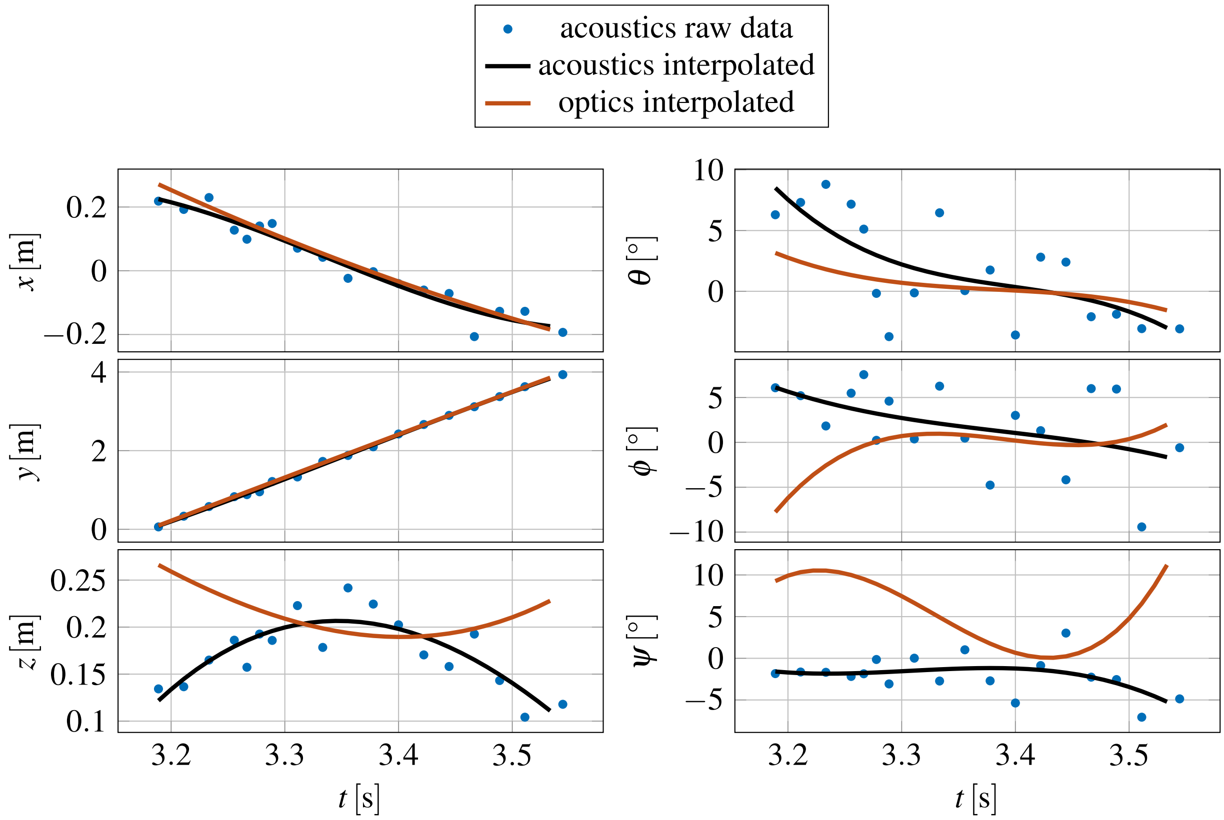

Figure 7: Translational (left) and rotational plot (right) of the acoustic tracking results (blue) and the "ground-truth" from the optical motion tracking (black) for a fast (10 m/s) fly-through.

4 CONCLUSION

This work presented a beamforming-based approach for short-range six-dimensional UAV tracking using microphone array measurements. In contrast to conventional acoustic tracking approaches, the proposed method incorporates both a dipole source model and coherent ground reflections. The resulting propagation model was integrated into a conventional frequency-domain beamforming framework and combined with an acoustic UAV model to estimate translational and rotational motion parameters.

The experimental validation was carried out using a large MEMS-based tracking array and an optical motion tracking system serving as a reference. The results demonstrate that the inclusion of dipole directivity and coherent ground reflections significantly improves localization accuracy compared to conventional monopole-based beamforming. In particular, the dipole model with reflections achieved the best agreement with the optical reference system for both slow and fast fly-throughs. For the slow flight case, a mean translational deviation of 3.8 cm and a rotational deviation of 6.5° were achieved. Even at higher flight speeds of 10 m/s, the proposed method maintained robust performance with translational errors close to 5 cm. The results further show that the dominant sound field of the investigated UAV can be represented reasonably well by a coherent dipole model including ground reflections.

The presented approach therefore demonstrates the feasibility of accurate acoustic 6 DoF tracking using microphone arrays alone, which is of particular interest for UAV noise measurements and future acoustic certification procedures. Since microphone arrays are already part of many aeroacoustic measurement setups, the proposed method enables simultaneous trajectory estimation and sound radiation analysis without requiring additional tracking hardware.

Nevertheless, several aspects offer potential for future improvement. The current dipole orientation is estimated using a simplified formulation and fixed pose assumptions. A promising extension would be the implementation of an inverse reconstruction algorithm that directly estimates the dipole pose and orientation from the measured cross-spectral matrix. Such an approach could improve especially the rotational accuracy and provide a more physically consistent reconstruction of the radiated sound field, although at the cost of increased computational complexity and runtime.

In addition, the investigated UAV sound field cannot always be described adequately by a pure dipole source. Future work should therefore consider hybrid source formulations combining monopole and dipole contributions and variations across different frequencies. Likewise, tilted or dynamically oriented dipoles should be included, as current research indicate that these become increasingly relevant during fast forward flight. More advanced propagation models, including frequency-dependent ground impedance and multiple reflections, may further improve localization accuracy in realistic outdoor environments.

Finally, the presented method should be validated for a broader range of UAV configurations, including different drone geometries, propeller types, flight maneuvers, payload conditions, and operating regimes. Extending the investigation to more complex trajectories and urban-like environments will be essential for assessing the robustness and applicability of the method for future UAV noise characterization and certification tasks.

References

[1] Acoustic Supplies. “Sound absorption coefficient chart (125 hz–4 khz).”, 2025. URL `https://www.acoustic-supplies.com/absorption-coefficient-chart/`, accessed: 2026-05-11.

[2] R. P. Dougherty. “Functional beamforming.” *Berlin Beamforming Conference*, 2004. URL `https://www.bebec.eu/fileadmin/bebec/downloads/bebec-2014/papers/BeBeC-2014-01.pdf`.

[3] EASA. “Study on the societal acceptance of urban air mobility in europe.”, 2021.

[4] EASA. “Guidelines on noise measurement of unmanned aircraft systems lighter than 600 kg operating in the specific category (low and medium risk).”, 2023.

[5] D. Ernst, R. Geisler, F. Philipp, T. Ahlefeldt, A. Goudarzi, and C. Spehr. “Enhancing aeroacoustic wind tunnel studies through massive channel upscaling with mems microphones.” In *Proceedings of AIAA/CEAS Aeronautics Conference*. American Institute of Aeronautics, 2024. doi:10.2514/6.2024-3064. URL `https://arc.aiaa.org/doi/10.2514/6.2024-3064`.

[6] Y.-J. Go and J.-S. Choi. “An investigation of multi-rotor drone noise based on the acoustic hemisphere in an actual environment.” *International Journal of Aeronautical and Space Sciences*, 25, 420–434, 2024. doi:10.1007/s42405-023-00697-y. URL `https://doi.org/10.1007/s42405-023-00697-y`.

[7] G. Herold. “In-flight directivity and sound power measurement of small-scale unmanned aerial systems.” *Acta Acustica*, 2022. doi:10.1051/aacus/2022052. URL `https://doi.org/10.1051/aacus/2022052`.

[8] Investing.com. “Globaler drohnenmarkt soll bis 2026 auf über 53 milliarden us-dollar wachsen.”, January 2026. URL `https://de.investing.com/news/company-news/globaler-drohnenmarkt-soll-bis-2026-auf-uber-53-milliarden-usdollar-wachsen-93CH-3444174`, accessed: 2026-04-25.

[9] C. Kawai, J. Jäggi, F. Georgiou, J. Meister, R. Pieren, and B. Schäffer. “Short-term noise annoyance towards drones and other transportation noise sources: A laboratory study.” *Journal of the Acoustical Society of America*, 156(4), 3037–3048, 2024. doi:10.1121/10.0026964.

[10] E. Sarradj. “Three-dimensional acoustic source mapping with different beamforming steering vector formulations.” *Advances in Acoustics and Vibration*, 2012(11), 1–12, 2012. doi:10.1155/2012/292695. URL `https://doi.org/10.1155/2012/292695`.

[11] B. Schäffer, R. Pieren, K. Heutschi, J. M. Wunderli, and S. Becker. “Drone noise emission characteristics and noise effects on humans—a systematic review.” *International Journal of Environmental Research and Public Health*, 18(11), 5940, 2021. doi:10.3390/ijerph18115940. URL `https://www.mdpi.com/1660-4601/18/11/5940`.

[12] P. Sijtsma. “Clean based on spatial source coherence.” *International Journal of Aeroacoustics*, 6(4), 357–374, 2007. doi:10.1260/147547207783359459. URL `https://doi.org/10.1260/147547207783359459`.

[13] L. Steinhoff and C. Spehr. “Akustisches uav-tracking in 6 freiheitsgraden fur direktionale schallabstrahlungsmessungen.” In *Proceedings of the DAGA 2026 Conference*. Deutsche Gesellschaft für Akustik e.V. (DEGA), 2026.